IEEE Photonics Journal
An IEEE Photonics Society Publication

Open Access

# Tunable Two-Section InAs/InP Quantum-Dash Laser: Numerical Modeling and Analysis

Volume 10, Number 6, December 2018

**Mohammed Zahed Mustafa Khan**, *Senior Member, IEEE*

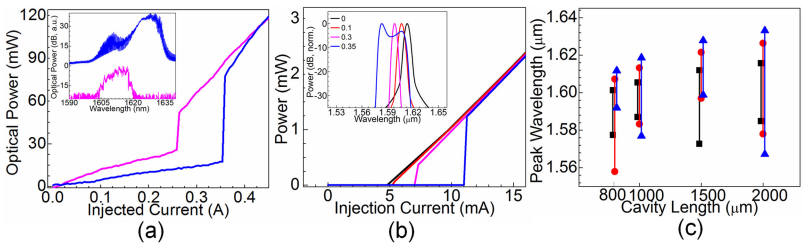


DOI: 10.1109/JPHOT.2018.2882444
1943-0655 © 2018 CCBY

# Tunable Two-Section InAs/InP Quantum-Dash Laser: Numerical Modeling and Analysis

**Mohammed Zahed Mustafa Khan**, ***Senior Member, IEEE***

Optoelectronics Research Laboratory, Electrical Engineering Department, King Fahd University of Petroleum and Minerals, Dhahran 31261, Saudi Arabia.

*DOI:10.1109/JPHOT.2018.2882444*


Manuscript received October 14, 2018; revised November 13, 2018; accepted November 15, 2018. Date of publication November 20, 2018; date of current version December 5, 2018. This work was supported by the Deanship of Research, King Fahd University of Petroleum and Minerals under Grant IN161029 and in part by King Abdulaziz City of Science and Technology under Grant EE2381 (KACST-TIC in Solid State Lighting).

**Abstract:** We report a multi-population rate-equation based numerical model for investigating broadband two-section InAs/InP quantum-dash laser. The model incorporates the quantum-wire-like nature of dashes along with the inhomogeneous broadening of the active region. Numerical results of light power–injection current and spectral characteristics at various absorber section lengths are shown to be in good agreement with the experimental results. Moreover, inhomogeneous broadening displayed a pivotal role in achieving large tunability from the monolithic two-section devices, in addition to demonstrating an extended lasing bandwidth. A blue-shift tuning window of 41.7 nm and bandwidth improvement of 18.5 nm is exhibited by 1000 $\mu$m cavity length device with largest active region inhomogeneity. In general, shorter 800–1000 $\mu$m and longer 2000 $\mu$m cavity length devices showed large wavelength tunability of 49 and 65 nm, respectively, in 1560–1640 nm wavelength region. This comprehensive analysis would enable design optimization of the tunable two-section devices that are considered potential key components in optical access networks.

**Index Terms:** Quantum-dash laser, monolithic tunable laser, broadband laser, rate-equation model.

## 1. Introduction

Tunable semiconductor lasers are indispensable components in numerous applications crossing multi-disciplinary fields, for instance, sensing, process control, and optical access networks in particular [1]. They are expected to play a crucial role in next-generation flexible wavelength division multiplexed based passive networks (WDM-PON). Moreover, monolithic devices have attracted attention as light sources owing to their compact feature and relatively simpler and reliable electrical tuning compared to external cavity tuning configuration. In this case, tunability is accomplished with a gain section and one or more tuning sections, which could be an absorber [1] or a partially pumped [2], [3] section, thus able to monolithically integrate (photonic integration) with other components of the communication system like modulators and amplifiers, [1], [4]. In recent years, modified multi-section devices with slotted [3]–[6] or coupled cavity [7], [8] structures, has been examined on InGaAsP/InP and AlGaAlAs/InP multiple quantum-well (Qwell) devices to extend the tuning range in excess of 40 nm in C-band wavelength window centered at ∼1550 nm, besides displaying a high side mode suppression ratio (SMR). In addition, monolithic multi-section lasers exhibiting

~45 nm tunability in ~1245–1290 nm range has also been reported in InAs/GaAs quantum-dot (Qdot) materials [9].

In the past few years, InAs/InP quantum-dash (Qdash) nanostructure active region-based amplifiers and lasers have demonstrated superior performances, compared to their Qwell and Qdot counterparts [10], thanks to their mixed quantum-wire and Qdot feature, and controlled emission tuning spanning from ~1400–1900 nm [11]. With these niche features, Qdash devices, and lasers in particular, are taking center stage in potential deployment in WDM systems that are expected to exhibit extended bandwidth up to L– and U – band, in next generation access networks [2]. L–band broadband laser, multi-wavelength laser, fiber-based tunable laser, and mode-locked lasers are few demonstrations from literature exploiting the unique wide gain profile of Qdashes owing to their inherent dispersive size during growth process, with notable performance. This substantiates the promise offered by this material system addressing the future source requirements [10]–[12].

In view of numerical modeling, several approaches have been presented on understanding the characteristics of Qwell slotted tunable laser structures. For instance, time-domain traveling-wave model [13], transition matrix method [14], combined scattering matrix and rate equation method [15], etc. On the other hand, rate equation models for Qdot lasers [16], [17], Qdash lasers [18], and two-section (gain–absorber) Qdot [19]–[21] and Qdash [22] mode-locked lasers have been studied comprehensively, but focusing mostly on mode-locking and pulse broadening characteristics. To the best of authors' knowledge, wavelength tuning characteristics of broadband Qdash laser have not yet been proposed and studied by theoretical models.

In this paper, we develop a simple rate equation model to simulate a two-section InAs/InP Qdash laser. The broad gain profile and homogeneous broadening of the active region are included in this model. The main tuning mechanism, which is the blue shift in the threshold gain peak with the absorber section length, is discussed in detail by altering the active region inhomogeneity of the system explicitly. The effects of the structure parameters on the tuning characteristics are also investigated in order to provide guidance for designing an optimized device. The simulation results reveal a tunability of as large as 49 and 65 nm covering C- and L-band from shorter 800–1000 $\mu$m and longer 2000 $\mu$m devices, respectively, thus affirming a promising source in next generation access networks with wider wavelength coverage. Besides large tunability, extended lasing bandwidth was also observed from the devices with large absorber section lengths and large active region inhomogeneity.

## 2. Multi-Population Rate Equation Model

The developed numerical model is based on linear optical gain analysis of InAs/InP Qdash laser active region with current injection [16], [18] that is formulated utilizing density matrix formulation. The resulting gain/absorption coefficient expressions are given by:

$$g_{G,m}^{j,k} = \frac{2\pi e^2 \hbar N_D}{c n_a \varepsilon_0 m_0^2} \frac{|M_{cv}|^2}{E_{cv}} \left(2P_{j,k}^{G} - 1\right) G_{j,k} B\left(E_m - E_{j,k}\right) \tag{1}$$

$$g_{A,m}^{j,k} = \frac{2\pi e^2 \hbar N_D}{c n_a \varepsilon_0 m_0^2} \frac{|M_{cv}|^2}{E_{cv}} \left(2P_{j,k}^{A} - 1\right) G_{j,k} B\left(E_m - E_{j,k}\right) \tag{2}$$

Here, Eqns. (1) and (2) represent the gain (loss) dynamics of the gain (absorber) section of the two-section Qdash laser diode with transition matrix element $|M_{cv}|^2$, and includes homogeneous $\hbar\Gamma_{\text{hom}}$ and inhomogeneous $\Gamma_{inh}$ broadenings of the active region in the form of Lorentzian and Gaussian distributions [18], respectively, as:

$$B\left(E_m - E_{j,k}\right) = \frac{0.16\hbar\Gamma_{\text{hom}}}{\left(E_m - E_{j,k}\right)^2 + \left(0.5\hbar\Gamma_{\text{hom}}\right)^2} \tag{3}$$

$$G_{j,k} = \frac{2.35}{\sqrt{2\pi}\Gamma_{inh}} \exp\left(\frac{\left(2.35(E_{j,0} - E_{cv})\right)^2}{2(\Gamma_{inh})^2}\right) dE_j \frac{\sqrt{E_{j,k+1} - E_{j,0}} - \sqrt{E_{j,k} - E_{j,0}}}{\sqrt{E_{j,N+1} - E_{j,0}}} \tag{4}$$

In Eqns. (1)–(4), the dispersive size of dashes are modeled as $j = 0, 1, 2, \ldots..2M_d$ groups with interband transition energy $E_{j,k} = E_{cv} - (M_d - j)\Delta E_j + k\Delta E_k$ where $E_{cv}$ is the central transition energy of $j = M_d$ dash group, and $k = 0, 1, 2, \ldots..N$ represents intradash energy level of each dash group, characterized by quantum-wire like nature with density of state (DOS) function $N_D$, given by:

$$N_D = A_{Dh}\sqrt{\frac{2m_e^*}{\pi^2\hbar^2}}\sqrt{E_{j,N+1} - E_{j,0}} \tag{5}$$

and Eqn. (4), where $A_{Dh}$ is the cross-sectional dash density. Moreover, in Eqns. (1)–(4), a series of longitudinal photon modes $m = 0, 1, 2, \ldots..M_p$ with energy $E_m = E_{cv} - (M_p - m)\Delta E_m$ are considered. Here, $\Delta E_m = ch/2n_aL$ is the mode spacing of the laser Fabry-Perot cavity of length $L$, stripe width $d$ and refractive index $n_a$. The carrier occupational probability of dash $E_{j,k}$ energy level, for the gain and absorber sections of respective lengths $L_G$ and $L_A$ are given by:

$$P_{j,k}^G = \frac{N_{j,k}^G}{2D_gN_DV_A^GG_{j,k}} \tag{6}$$

$$P_{j,k}^A = \frac{N_{j,k}^A}{2D_gN_DV_A^AG_{j,k}}, \tag{7}$$

Where $V_A^G = 0.75N_{lyr}h_{Dh}dL_G$ and $V_A^A = 0.75N_{lyr}h_{Dh}dL_A$ are the active region volume of the gain and absorber section, respectively, with $N_{lyr}$ dash layers with an average $h_{Dh}$ ($w_{Dh}$) height (width) [18]. $N_{j,k}^G$ and $N_{j,k}^A$ are the corresponding dash ground state (GS) carrier populations of the two-section device with degeneracy $D_g$. Two more energy levels are considered in the model; the reservoir of carriers i.e., separate confinement heterostructure (SCH), from which carriers relax into wetting layer (WL), and finally into the dash GS energy level. The relaxation $\tau_{SW}$ ($SCH \rightarrow WL$), $\tau_{WD}$ ($WL \rightarrow GS$), re-excitation $\tau_{WS}$ ($WL \rightarrow SCH$), $\tau_{DW}$ ($GS \rightarrow WL$), and recombination $\tau_S$ ($SCH$), $\tau_W$ ($WL$) and $\tau_D$ ($GS$) are the associated time constants of the three energy-level system. The resulting carrier–carrier and carrier–photon rate equations in the gain section of the system are as follows:

$$\frac{dN_{SCH}^G}{dt} = \frac{\eta_i I_G}{e} - \frac{N_{SCH}^G}{\tau_{SW}} - \frac{N_{SCH}^G}{\tau_S} + \frac{N_{WL}^G}{\tau_{WS}} \tag{8a}$$

$$\frac{dN_{WL}^G}{dt} = \frac{N_{SCH}^G}{\tau_{SW}} + \sum_{j,k}\frac{N_{j,k}^G}{\tau_{G-DW}^{j,k}} - \frac{N_{WL}^G}{\overline{\tau}_{G-WD}} - \frac{N_{WL}^G}{\tau_{WS}} - \frac{N_{WL}^G}{\tau_W} \tag{8b}$$

$$\frac{dN_{j,k}^G}{dt} = \frac{N_{WL}^GG_{j,k}}{\tau_{G-WD}^{j,k}} - \frac{N_{j,k}^G}{\tau_{G-DW}^{j,k}} - \frac{N_{j,k}^G}{\tau_D} - \frac{c\Gamma}{n_a}\sum_m\frac{L_G}{L}g_{G,m}^{j,k}\,S_m \tag{8c}$$

Where $\eta_i$ and $I_G$ are the injection efficiency and the gain current, respectively. The average $\overline{\tau}_{G-DW}$ and local $\tau_{G-DW}^{j,k}$ carrier escape rates from dash GS to WL are calculated from the initial capture rate $\tau_{WD0}$ at absolute temperature $T$, in the following ways:

$$\frac{1}{\overline{\tau}_{G-DW}} = \sum_{j,k}\frac{G_{j,k}}{\tau_{G-WD}^{j,k}} = \sum_{j,k}\frac{G_{j,k}\left(1 - P_{j,k}^G\right)}{\tau_{WD0}} \tag{9a}$$

$$\frac{1}{\tau_{G-DW}^{j,k}} = \left(1 - \frac{N_{WL}^G}{2D_wV_W^G}\right)\left(\frac{D_wV_W^G}{D_gN_DV_A^G}\right)\tau_{WD0}^{-1}\exp\left(\frac{E_{j,k} - E_{wl}}{kT}\right) \tag{9b}$$

In Eqn. 9(b), $E_{wl}$ is WL energy with degeneracy $D_w$ and gain section volume $V_W^G = w_{WL}\,dL_G$. Now, replacing $N_{SCH}^G$, $N_{WL}^G$, $N_{j,k}^G$, $L_G$, $g_{G,m}^{j,k}$, and $I_G$ with $N_{SCH}^A$, $N_{WL}^A$, $N_{j,k}^A$, $L_A$, $g_{A,m}^{j,k}$ and $I_A$, respectively, in Eqn. 8, yields another set of carrier-photon rate equations describing the dynamics of the absorber section. Note that, in this case, $I_A = 0$ until and unless specified. The carrier escape rates from GS to WL in absorber section can be calculated in a similar manner by replacing $\overline{\tau}_{G-WD}$, $\tau_{G-DW}^{j,k}$,

$P^G_{j,k}$, $N^G_{WL}$, $V^G_W$ and $V^G_A$, in Eqn. 9, with $\overline{\tau}_{A-WD}$, $\tau^{j,k}_{A-DW}$, $P^A_{j,k}$, $N^A_{WL}$, $V^A_W = w_{WL}\, dL_A$ and $V^A_A$, respectively. Finally, the coupled multimode photon rate equation with population $S_m$, is, therefore, given by:

$$\frac{dS_m}{dt} = \frac{\beta}{\tau_{Sp}} \sum_{j,k} B\left(E_m - E_{j,k}\right) N^G_{j,k} + \frac{c\Gamma}{n_a} \sum_{j,k} \left( \frac{L_G}{L} g^{j,k}_{G,m} + \frac{L_A}{L} g^{j,k}_{A,m} \right) S_m - \frac{S_m}{\tau_P} \tag{10}$$

The first term on the right hand side of Eqn. 10 represents the spontaneous emission term with emission life time $\tau_{Sp}$, while the last two terms are the stimulated emission and photon loss, with photon lifetime $\tau_P = (c/n_a)(\alpha_i + \ln(1/R_1R_2)/2L)$. The internal loss of the medium and the facet reflectivities of the laser cavity are respectively, $\alpha_i$, $R_1$ and $R_2$. It is worth mentioning that Eqn. 8(c) and corresponding absorber rate equation, along with Eqn. 10, couples the dynamics of gain and absorber section.

The complete set of rate equations; Eqn. 8 for the gain section and corresponding equations for absorber section, and Eqn. 10, are then solved using fourth-order Runge-Kutta method by applying current at time $t = 0$, and then obtain steady state solutions of the carrier and photon populations in the gain and absorber sections. Thereafter, the laser output power of the $m^{th}$ longitudinal mode of photon energy $\hbar\omega_m$ from one facet is obtained by [16], [18]:

$$I_m = \hbar\omega_m c S_m \ln(1/R)/2Ln_a \tag{11}$$

## 3. Results and Discussion

Using the set of rate equations, the laser optical power and light-emission characteristics of the monolithic two-section InAs/InP Qdash laser diode is analyzed for wavelength tunability assuming all carriers are available in the SCH laser and injected into the WL layer, i.e., $\eta_i = 1$ and $\tau_S = \infty$. The values of other time constants utilized in the simulation are $\tau_{Sp} = 2.8$ ns, $\tau_W = 0.8$ ns, $\tau_D = 0.5$ ns, $\tau_{SW} = 0.5$ ns, $\tau_{WS} = 1.0$ ns and $\tau_{WD0} = 2.0$ ps [18]. The homogeneous broadening, spontaneous emission coupling efficiency and the optical confinement factor of the active region are $\hbar\Gamma_{\text{hom}} = 10$ meV, $\beta = 10^{-4}$ and $\Gamma = 0.03$, respectively [18]. The considered InAs/InP Qdash laser devices consists of $N_{lyr} = 4$ layer of dashes with corresponding mean height, width and cross-section density $h_{Dh} = 1.5$ nm, $w_{Dh} = 20$ nm and $A_{Dh} = 7.9 \times 10^{-13}$cm$^2$, and SCH (WL) thickness $w_{SCH} = 100$ nm ($w_{WL} = 5$ nm). The device has a strip width $d = 3$ $\mu$m, facet reflectivies $R_1 = R_2 = 0.3$, and internal loss $\alpha_i = 7.5$ cm$^{-1}$.

The other parameters used in the model are as follows: degeneracy of the SCH, WL, and GS are taken as $D_{SCH} = 4.8 \times 10^{20}$cm$^{-3}$, $D_{WL} = 1.7 \times 10^{19}$cm$^{-3}$ and $D_G = 1$. The dash density of states $N_D = 13 \times 10^{17}$cm$^{-3}$, central transition energy $E_{cv} = 790$ meV, WL and SCH layer energies $E_{wl} = 990$ meV and $E_{sch} = 1140$ meV. The transition matrix values are extracted from [19]. The dash group separation is fixed at $\Delta E_j = 0.354$ meV while the number of groups $2M_d$, inhomogeneous broadening $\Gamma_{inh}$ and gain (absorber) section length $L_G(L_A)$ are varied to investigate the wavelength tunability of the two-section laser device.

### 3.1 Effect of Absorber Length on L–I and Spectral Characteristics

Fig. 1(a) depicts the simulated optical power – injection current ($L$–$I$) characteristics of the two-section laser device at a fixed cavity length $L = 1000$ $\mu$m and inhomogeneous broadening of the active region $\Gamma_{inh} = 75$ meV. Here, the injection current corresponds to the current $I_G$ of the pumped (gain) section while the absorber section is left unpumped ($I_A = 0$). For analysis purpose, we vary the absorber section length according to $L_A/L$ ratio, from 0 to 0.35, where 0 corresponds to a single section device without an absorber section. A linear rise in the threshold current $I_{th}$ is observed up to $L_A/L = 0.2$ whereas the value surges abruptly for $L_A/L \geq 0.3$ following a near-exponential trend with a sharp turn-on behavior. For instance, an abrupt increase in $I_{th}$ (optical power) from 5.8 mA (0.08 mW) to 11.2 mA (1.24 mW) is observed when $L_A$ is enlarged from 200 to 350 $\mu$m, as illustrated in Fig. 1(a). This is ascribed to the alteration in the absorption loss of the system, and

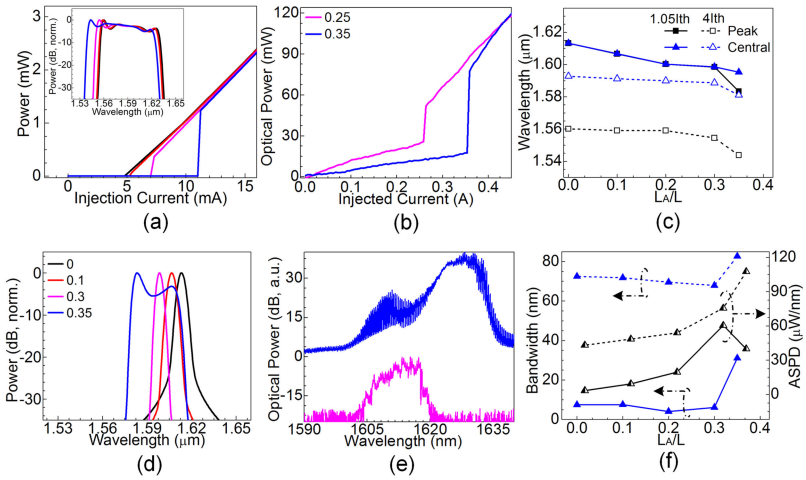


Fig. 1. Room temperature simulated, (a) and (d), and experimental, (b) and (e), *L–I* characteristics and lasing spectra at $1.05I_{th}$ of the two-section InAs/InP Qdash laser, respectively. Variation of (c) $\lambda_p$ and $\lambda_c$, and (f) $\Delta\lambda$ and ASPD at $1.05I_{th}$ (solid line) and $4I_{th}$ (dashed line). The inset of (a) shows the lasing spectrum at $4I_{th}$. Legends of (b) and (d) show $L_A/L$ values. The spectra of (e) are offset along y-axis for clarity.

we explain this observation qualitatively by considering the following threshold gain equation:

$$\Gamma g_{th} = (\alpha_i + \ln(1/R_1R_2)/2L) = (\alpha_i + \alpha_m) = \Gamma\left[\frac{L_G}{L}g_G + \frac{L_A}{L}g_A\right] \tag{12}$$

At comparatively smaller $L_A/L$ value of $\leq 0.2$, the resulting enhancement in absorption loss $g_A$ due to longer absorption section length, contributes gradually to the total loss $(\alpha_i + \alpha_m)$ of the system, and hence a steady increase of injected carriers in the shorter length pumped section, is required to attain gain threshold $g_{th}$. Nonetheless, in the case of $L_A/L \geq 0.3$, the absorption loss $g_A$ has escalated further due to even longer $L_A$ but the associated additional reduction in the gain section now requires a high influx of carriers to generate considerable $g_G$ and thus amplified spontaneous emission (ASE) to totally bleach the high absorption loss of the unpumped section [23] and reach $g_{th}$, as dictated by Eqn. (12). Hence, this intense current pumping process at larger $L_A/L$ is attributed to the observed sharp turn-on behavior in Fig. 1(a), which was not visible at smaller absorber section lengths. Moreover, this peculiar characteristic is also accompanied with the wavelength blue shifting and lasing emission broadening at threshold ($1.05I_{th}$) as shown in Fig. 1(d), in particular, at $L_A/L = 0.35$. This is ascribed to increased occupancy of higher transition energies and more dispersive energy states of Qdashes with the intense surge of carriers at larger $L_A/L$, to compensate for the enhanced absorption loss of the system. In this case, simultaneous lasing from smaller (higher transition energy) and larger (small transition energy) average height dash ensembles, with shorter dashes dominating, results in blue shifting as well as broadening the lasing spectra. This is possible in an inhomogeneous system since smaller dashes possess dot-like features with a lower modal gain compared to larger dashes with a higher modal gain [10], [18].

In order to ascertain our findings, we have compared the simulation results with our very recent experimental results of two-section InAs/InP Qdash lasers with $L = 930$ $\mu$m, $L_A/L = 0.25$ and 0.35 and shown in Figs. 1(b) and (e). More details about the device structure could be found in reference [10], [12]. A very analogous trend of sharp turn-on behavior with elevated threshold optical power as well as $I_{th}$ (77 mW at 0.36 A compared to 52 mW at 0.26 A) is observed on increasing $L_A$, as illustrated in Fig. 1(b). Correspondingly, a good agreement between the experimental and the simulated lasing spectra at $1.05I_{th}$, is apparent on comparing Figs. 1(d) and (e). While experimental lasing $-12$ dB bandwidth of 14 and 24 nm is measured at $L_A/L = 0.25$ and 0.35, respectively, the simulation results reproduced this trend noticeably by exhibiting $-6$ dB bandwidth ($\Delta\lambda$) values 6.1

and 31.1 nm values. Hence, these results affirm the effective modeling of the two-section InAs/InP Qdash laser by our developed model. It is to be noted that $I_{th}$ and the lasing emission coverage values, predicted by the model, are different from that of the experiments (see Fig. 1). This is expected because the utilized laser devices in these cases are different. The objective here is to predict the trend in *L–I* characteristics and lasing spectra, and not to accurately model the energy states and other dynamics of Qdash active region.

Notice that, both, simulated and experimental lasing spectra show an asymmetric-top profile as depicted by Figs. 1(d) and (e). In addition, Fig. 1(d) shows wavelength peak $\lambda_p$ at the shorter wavelengths, which is attributed, in part, to the spectral hole burning and shift of gain maxima towards the shorter wavelength, and to the shorter dashes dominating the lasing process, discussed above. On the other front, Fig. 1(e) shows a contrasting behavior from the experimental results wherein $\lambda_p$ moved to longer wavelength, suggesting dominance by larger dash (smaller transition energies) ensemble. This could be possible due to device junction heating at high carrier injection in large $L_A/L$ devices, assisting thermal carrier leakage from higher transition energies of smaller dashes with small band offsets. In such scenarios, the lasing bandwidth is balanced by emissions from both smaller and larger dashes with larger dashes (hence longer wavelength emission) dominating. Therefore, in addition to $\lambda_p$, we have also considered $\Delta\lambda$ at $-6$ dB optical power and $\lambda_c$ as the corresponding central lasing wavelength for the analysis of the two-section device, which is reasonable to minimize the effect of asymmetric-top on the calculations. In particular, we considered both $\lambda_c$ and $\lambda_p$ in our investigation of the blue shift phenomenon since this essentially dictates the two-section device tunability.

As expected from the inhomogeneous nature of the Qdash active region, a typical broadening of the lasing spectrum is observed above threshold, and the inset of Fig. 1(a) plots the simulated lasing spectra at $4I_{th}$ of the two-section device as a function of $L_A/L$. A summary of the calculated results at various $L_A/L$ values is shown in Figs. 1(c) and (f) for $1.05I_{th}$ and $4I_{th}$ injection current values. As expected from our previous analysis, blue shifting of $\lambda_c$ and $\lambda_p$ are also observed at $4I_{th}$, on increasing $L_A$ besides an appreciable variation between them due to the asymmetric-top profile of the lasing bandwidth. Nevertheless, from Fig. 1(f), $\Delta\lambda$ at $4I_{th}(1.05I_{th})$ is measured to be 82 (31.1) nm for a $L_A = 350$ $\mu$m compared to 72 (6.1) nm from a single section device ($L_A = 0$). The resulting $\lambda_p$ ($\lambda_c$) of the two-section and single-section devices at $1.05I_{th}$ are 1583.4 (1595.3) nm and 1.613.2 (1.613.2) nm, respectively, with corresponding total blue shift wavelength tunability of 29.8 nm and 17.9 nm, respectively. Moreover, it is noteworthy to mention that an average spectral power density (ASPD), calculated as the ratio of $\Delta\lambda$ and the optical power, is found to be considerably large for $L_A/L = 0.35$ device, reaching as high as 39.8 (107.6) $\mu$W/nm at $1.05I_{th}(4I_{th})$. Hence, this analysis, along with extended bandwidth achievement of 10 nm from the two-section device compared to a single-section device at $4I_{th}$, supports potential employment of two-section Qdash laser device as a light source in next-generation optical access networks.

### 3.2 Effect of Active Region Inhomogeneity

Figs. 2(a)–(b) shows the *L–I* characteristics at $L_A/L = 0.35$ and the change in $I_{th}$ across various $L_A/L$ values, for the 1000 $\mu$m two-section device, and as a function of an explicit increase in the active region inhomogeneity $\Gamma_{inh}$. The remaining laser structure parameters are unaltered. Besides demonstrating a rising near-exponential relation between $I_{th}$ and $L_A$, which has been discussed in the previous section, a further boost in $I_{th}$ from 5.0 to 5.3 mA is observed from Fig. 2(b) on explicitly enhancing $\Gamma_{inh}$ by 25 meV of the single section device. While this steady growth is observed for $L_A/L \leq 0.2$, a significant rise in $I_{th}$ is apparent from $L_A/L \geq 0.3$ devices. Moreover, this behavior is found to intensify with $I_{th}$ reaching as high as 14 mA at $\Gamma_{inh} = 85$ meV compared to 8.8 mA at $\Gamma_{inh} = 60$ meV, for $L_A = 350$ $\mu$m device. This is ascribed to an additional loss mechanism occurring in the system due to extended active region inhomogeneity i.e., carrier feeding process via optical pumping, where the generated high energy photons by smaller dashes getting absorbed by larger dashes with smaller transition energies to attain population inversion [18]. In this scenario, this re-absorption loss mechanism competes with the absorption loss of the unpumped section, thus

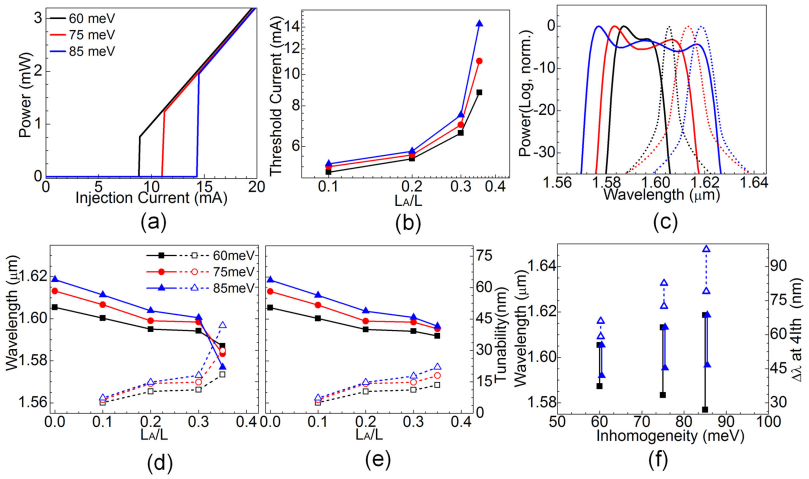


Fig. 2. Effect of $\Gamma_{inh}$ on the room temperature simulated (a) *L–I* characteristics and (b) $I_{th}$, of the two-section 1000 $\mu$m InAs/InP Qdash laser, at $L_A/L = 0.35$ and variable $L_A/L$ values, respectively. The corresponding calculated (c) lasing spectra at $1.05I_{th}$ for $L_A/L = 0$ (dotted line) and 0.35 (solid line), and (d) $\lambda_p$ and (e) $\lambda_c$ with respective tunability, at different $\Gamma_{inh}$ values. (f) Summary of total $\lambda_p$ (black solid line) and $\lambda_c$ (blue solid line) wavelength shift (tunability), and $4I_{th}$ $\Delta\lambda$ (dashed blue line), between $L_A/L = 0$ and $L_A/L = 0.35$.

altering the total loss of the system and hence $g_{th}$ of Eqn. 12. A typical red shift in the lasing spectrum, $\lambda_p$ and $\lambda_c$ at $1.05I_{th}$, plotted in Figs. 2(c)–(e), respectively, is observed from the single section device with enlarging $\Gamma_{inh}$ by 25 meV, which is a signature of enhanced active region inhomogeneity of the system. However, on further extending the absorber section length, this red shift phenomenon is found to shrink and reaches similar values at $L_A/L = 0.3$ (0.35) for $\lambda_p$ ($\lambda_c$). This indicates an intense competition between the two loss mechanisms happening in the system since absorption loss due to $L_A$ blue shifts the lasing spectrum (see Figs. 1(a) and (d)). Increasing $L_A/L$ value is associated with longer absorber-section lengths and shorter pumped section length. As a result, this shorter $L_G$ now needs to compensate for its own and $L_A$'s additional photon re-absorption loss, as well as the absorption loss of $L_A$ that has already escalated due to the longer length. This requires a considerable surge of carriers in the gain section to generate $g_G$ so as to compensate for an inherent soar in $\alpha_i$, and rise in $g_A$, to reach $g_{th}$ or the onset of lasing. Hence, more carrier occupancy in the higher energy states of the shorter dashes tends to slowly mask the photon re-absorption by longer dashes by simultaneous feeding larger dash ensembles and the active region of the absorber section. This mechanism gradually reduces the red shift phenomenon in Figs. 2(d) and (e) with increasing $\Gamma_{inh}$ and $L_A/L$, and subsequently significant emission from smaller dash ensemble results in comparable $\lambda_c$ at $L_A/L = 0.35$ while $\lambda_p$ experiences large blue shift and hence crossover of values. This implies consideration of both the wavelengths is required to understand the tuning characteristics of the two-section Qdash laser. Here, we define tuning as the blue shift of the whole broadband lasing spectrum by altering the gain profile of the two-section device via the absorption coefficient of the unpumped section, according to Eqn. (12).

Another noted influence of $\Gamma_{inh}$ is the intense sharp turn-on behavior in the *L–I* characteristics (Fig. 2(a)) and broadening of the lasing spectrum at threshold (Fig. 2(c)) for $L_A/L = 0.35$. Besides an increase in $I_{th}$, the optical power at threshold ($1.05I_{th}$) and $\Delta\lambda$ enhanced considerably with extended $\Gamma_{inh}$ values. In fact, the optical power and $\Delta\lambda$ at 85 meV are found to be more than doubled (1.98 mW and 46.3 nm) compared to 0.76 mW and 16.5 nm, respectively, at 60 meV. We attribute this observation yet again to the severe bleaching effect, as discussed above, by generating more ASE to completely compensate the absorption of the unpumped section as well as the additional photon re-absorption loss due to extended $\Gamma_{inh}$. As a consequence, simultaneous stimulated emission from smaller and larger average dash height groups is expected at large $\Gamma_{inh}$ values, thus broadening the lasing spectrum.

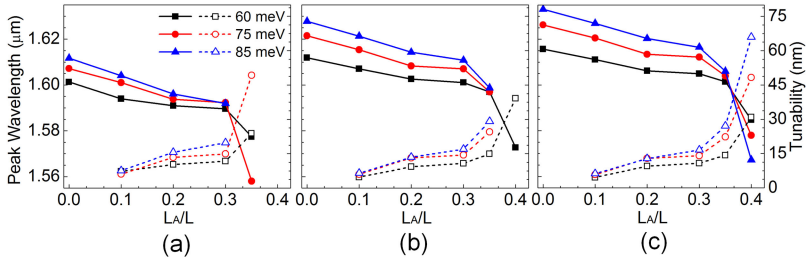


Fig. 3. Effect of $\Gamma_{inh}$ on the room temperature calculated $\lambda_p$ and the resultant blue shift with respect to single section ($L_A/L = 0$) device (wavelength tunability), of the two-section InAs/InP Qdash laser at (a) $L = 800$ $\mu$m, (b) $L = 1000$ $\mu$m, and (c) $L = 2000$ $\mu$m.

Fig. 2(f) summarizes the entire characteristics of 1000 $\mu$m laser two-section laser diode by plotting the effect of $\Gamma_{inh}$ on the threshold ($1.05I_{th}$) $\lambda_p$ and $\lambda_c$ and the corresponding wavelength shift at various values of $L_A$, which are calculated with reference to the single section device. In general, the device $\lambda_p$ tunability enhances with the absorber section length, and device with $L_A/L = 0.35$ demonstrated the largest blue shift of 41.7 nm (1576.9 nm compared to 1618.6 nm for $L_A/L = 0$) at $\Gamma_{inh} = 85$ meV, as shown in Figs. 2(d) and (f). On the other hand, a blue shift of 22 nm (1596.6 nm compared to 1618.6 nm) is displayed by the device should $\lambda_c$ is considered (see Figs. 2(e) and (f)). Apart from wavelength tunability, the two-section device also demonstrated improved $\Delta\lambda$ by 18.5 nm (97.5 nm at $L_A = 350$ $\mu$m compared to 79 nm at $L_A = 0$) at $4I_{th}$ and an extended active region inhomogeneity $\Gamma_{inh} = 85$ meV. Hence, a comprehensive analysis of the two-section laser diode displayed three-fold benefits; wavelength tunability, extended $\Delta\lambda$, and high ASPD, compared to the single section counterpart.

### 3.3 Effect of Cavity Length

In this section, we varied the cavity length L of the two-section InAs/InP Qdash laser to understand its effect on the tuning and broadband emission characteristics, while varying $L_A/L$ and $\Gamma_{inh}$ values and keeping the remaining laser device parameters unaltered. The calculated results of $\lambda_p$ and its respective shift (compared to single section device) at $1.05I_{th}$, are displayed in Figs. 3(a)–(c) for three cavity lengths L = 800, 1500 and 2000 $\mu$m, respectively. Comparing their performance alongside 1000 $\mu$m device (Fig. 2(d)), a total $\lambda_p$ red shift and tunability, across various $\Gamma_{inh}$ values, are found to show contrasting behavior across the cavity lengths. Shrinking of the red shift phenomenon (due to enlarged $\Gamma_{inh}$) is observed at an early value of $L_A/L = 0.3$ for shorter cavity lengths ($L \leq 1000$ $\mu$m) compared to $L_A/L = 0.35$ for longer cavity lengths ($L \geq 1500$ $\mu$m), while the device tunability enhanced with increasing $L_A/L$ for all cavity length devices, as depicted by Fig. 3. Furthermore, shorter $L = 800$ $\mu$m device at $L_A/L = 0.35$ cease lasing with an extended inhomogeneity of $\Gamma_{inh} = 85$ meV. This is an indication of gain saturation of the pumped section and hence inability to generate the required $g_G$ to reach the already high $g_{th}$, which is due to the shorter cavity length (larger mirror loss $\alpha_m$, see Eqn. 12) and additional loss in the form of an implicit increase in $\alpha_i$ caused by large $\Gamma_{inh}$. On the contrary, longer $L = 1500$ $\mu$m length device lased at large $L_A/L = 0.4$ value only at the smaller inhomogeneous broadening of $\Gamma_{inh} = 60$ meV. Thanks to the inherent reduction in the total loss of the system (i.e., implicit decrease in $\alpha_i$ due to small $\Gamma_{inh}$ value as well as smaller $g_{th}$ due to the longer cavity) which enabled the pumped section to provide sufficient gain $g_G$ to reach $g_{th}$. It is noteworthy to mention that a similar behavior of tunability and wavelength shift, shown in Fig. 2(e) for $L = 1000$ $\mu$m, was also observed with $\lambda_c$, across the other cavity lengths.

Lastly, we summarize the comprehensive analysis of the wavelength tunability of InAs/InP Qdash two-section laser and show $\lambda_p$ and $\lambda_c$ for the single section device and the device exhibiting the largest blue shift (i.e., largest $L_A$ and $\Gamma_{inh}$ combination that sustained lasing), in Figs. 4(a) and 4(b), respectively. Considering $\lambda_p$, the largest tunability of 65 nm is demonstrated by the longest cavity $L = 2000$ $\mu$m device at $\Gamma_{inh} = 85$ meV, followed by 49 nm from the shortest 800 $\mu$m cavity laser at

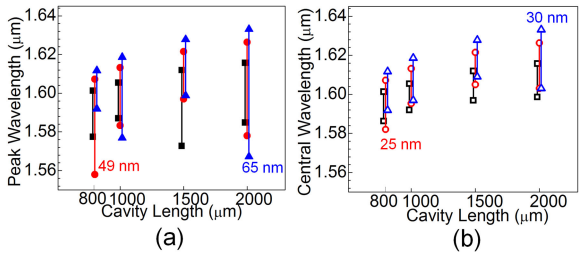


Fig. 4. Summary of the two-section InAs/InP Qdash laser device wavelength tunability as a function of $L$ and $\Gamma_{inh}$. Total (a) $\lambda_p$ and (b) $\lambda_c$ wavelength shift between $L_A/L = 0$ and maximum achievable $L_A/L$ and $\Gamma_{inh}$ values that sustained lasing. The numbers in (a) and (b) correspond to the largest tunability achieved from the longer and the shorter cavity length devices. The solid line colors follow the legend of Fig. 3.

$\Gamma_{inh} = 75$ meV. On the other hand, tunability of 25 (30) nm is displayed by 800 (2000) $\mu$m cavity device at $\Gamma_{inh} = 75$ meV and 85 meV, respectively, should $\lambda_c$ be regarded. In either case, notice that shorter and comparatively longer cavity two-section devices are the better options to exploit the complete gain-bandwidth of the active region for tunability.

## 4. Conclusion

We have comprehensively investigated the characteristics of a two-section InAs/InP quantum-dash laser, in particular, the wavelength tuning capability, by a newly developed theoretical model. The numerical technique incorporates the carrier-photon dynamics of an absorber and the gain section in the form of multi-population rate equations. A large blue shift wavelength tuning is observed from the shorter and longer cavity length devices, reaching a value of 49 and 65 nm, respectively, covering both C- and L-band wavelength region. Moreover, and extended bandwidth of 18.5 nm is also exhibited by the two-section device compared to the single section counterpart, affirming the potential of two-section InAs/InP Qdash laser light source in a plethora of multi-disciplinary field applications, and optical access networks in particular.

## Acknowledgment

The author thanks E. Alkhazraji for sharing the experimental results and Dr. Mohd Sharizal Alias for fabrication of the two-section devices.

## References

[1] L. A. Coldren, "Monolithic tunable diode lasers," *IEEE J. Sel. Topics Quantum Electron.*, vol. 6, no. 6, pp. 988–999, Nov./Dec. 2000.
[2] K. Liu, S. X. Mu, Y. Lu, B. L. Guan, and E. Y. B. Pun, "L-band wavelength-tunable MQW Fabry–Pérot laser using a three-segment structure," *IEEE Photon. Technol. Lett.*, vol. 25, no. 18, pp. 1754–1757, Sep. 2013.
[3] A.-H. Kim, J.-H. Park, H.-S. Cho, and C.-H. Lee, "Laser spectral envelope control using a double contact Fabry-Perot laser diode for WDM-PON," *IEEE Photon. Technol. Lett.*, vol. 18, no. 20, pp. 2132–2134, Oct. 2006.
[4] D. C. Byrne *et al.*, "Discretely tunable semiconductor lasers suitable for photonic integration," *IEEE J. Sel. Topics Quantum Electron.*, vol. 15, no. 3, pp. 482–487, May/Jun. 2009.
[5] J. P. Engelstaedter, B. Roycroft, F. H. Peters, and B. Corbett, "Wavelength tunable laser using an interleaved rear reflector," *IEEE Photon. Technol. Lett.*, vol. 22, no. 1, pp. 54–56, Jan. 2010.
[6] F. Smyth, E. Connolly, B. Roycroft, B. Corbett, P. Lambkin, and L. P. Barry, "Fast wavelength switching lasers using two-section slotted Fabry–Perot structures," *IEEE Photon. Technol. Lett.*, vol. 18, no. 20, pp. 2105–2107, Oct. 2006.
[7] Y. Wang, Y. Yang, and J.-J. He, "Single-electrode controlled four-section coupled-cavity tunable laser," *IEEE Photon. Technol. Lett.*, vol. 25, no. 14, pp. 1340–1343, Jul. 2013.
[8] J. Jin, L. Wang, T. Yu, Y. Wang, and J.-J. He, "Widely wavelength switchable v-coupled-cavity semiconductor laser with 40 dB side-mode suppression ratio," *Opt. Lett.*, vol. 36, no. 21, pp. 4230–4232, 2011.
[9] D. I. Nikitichev *et al.*, "High-power wavelength bistability and tunability in passively mode-locked quantum-dot laser," *IEEE J. Sel. Topics Quantum Electron.*, vol. 19, no. 4, , Jul./Aug. 2013, Art. no. 1100907.

[10] M. Z. M. Khan, T. K. Ng, and B. S. Ooi, "Self-assembled InAs/InP quantum dots and quantum dashes: Material structures and devices," *Prog. Quantum Electron.*, vol. 38, no. 6, pp. 237–313, 2014.
[11] J. P. Reithmaier, G. Eisenstein, and A. Forchel, "InAs/InP quantum-dash lasers and amplifiers," *Proc. IEEE*, vol. 95, no. 9, pp. 1779–1790, Sep. 2007.
[12] M. A. Shemis *et al.*, "Broadly tunable self-injection locked InAs/InP quantum-dash laser based fiber/FSO/hybrid fiber-FSO communication at 1610 nm," *IEEE Photon. J.*, vol. 10, no. 2, Apr. 2018, Art. no. 7902210.
[13] J. Zhao, K. Shi, Y. Yu, and L. P. Barry, "Theoretical analysis of tunable three-section slotted fabry–perot lasers based on time-domain traveling-wave model," *IEEE J. Sel. Topics Quantum Electron.*, vol. 19, no. 5, pp. 1–8, Sep./Oct. 2013.
[14] Y. Li, Y. Xi, X. Li, and W.-P. Huang, "Design and analysis of single mode fabry-perot lasers with high speed modulation capability," *Opt. Exp.*, vol. 19, no. 13, pp. 12131–12140, 2011.
[15] Q. Y. Lu *et al.*, "Analysis of slot characteristics in slotted single-mode semiconductor lasers using the 2-D scattering matrix method," *IEEE Photon. Technol. Lett.*, vol. 18, no. 24, pp. 2605–2607, Dec. 2006.
[16] M. Sugawara, K. Mukai, Y. Nakata, H. Ishikawa, and A. Sakamoto, "Effect of homogeneous broadening of optical gain on lasing spectra in self-assembled In_{x}Ga_{1−x}As/GaAs quantum dot lasers," *Physical Rev. B*, vol. 61, no. 11, 2000, Art. no. 7595.
[17] M. Kashiri and A. Asgari, "Modeling of carrier dynamics in InGaAs/GaAs self-assembled quantum dot lasers," *Appl. Opt.*, vol. 55, no. 8, pp. 2042–2048, 2016.
[18] M. Z. M. Khan, T. K. Ng, U. Schwingenschlogl, and B. S. Ooi, "Spectral analysis of quantum-dash lasers: Effect of inhomogeneous broadening of the active-gain region," *IEEE J. Quantum Electron.*, vol. 48, no. 5, pp. 608–615, May 2012.
[19] M. Radziunas, A. G. Vladimirov, E. A. Viktorov, G. Fiol, H. Schmeckebier, and D. Bimberg, "Pulse broadening in quantum-dot mode-locked semiconductor lasers: Simulation, analysis, and experiments," *IEEE J. Quantum Electron.*, vol. 47, no. 7, pp. 935–943, Jul. 2011.
[20] H. Simos *et al.*, "Numerical analysis of passively mode-locked quantum-dot lasers with absorber section at the low-reflectivity output facet," *IEEE J. Quantum Electron.*, vol. 49, no. 1, pp. 3–10, Jan. 2013.
[21] J. Rahimi, V. Ahmadi, and M. H. Yavari, "Modeling and analysis of distributed feedback quantum dot passively mode-locked lasers," *Appl. Opt.*, vol. 55, no. 19, pp. 5102–5109, 2016.
[22] C-Y. Lin, Y-C. Xin, Y. Li, F. L. Chiragh, and L. F. Lester, "Cavity design and characteristics of monolithic long-wavelength InAs/InP quantum dash passively mode-locked lasers," *Opt. Exp.*, vol. 17, no. 22, pp. 19739–19748, 2009.
[23] J. Le and P. Zory, "Sharp turn-on diode lasers," in *Proc. 16th Annu. Meet. IEEE Lasers Electro-Opt. Soc.*, 2003, vol. 2, pp. 987–988.